doi:10.26443/seismica.v2i4.1559

Tectonic tremor: The chatter of mafic underplating

Geena F. Littel [1], **Michael G. Bostock** [*1], **Charles G. Sammis** [1], **Simon M. Peacock** [1], **Andrew Calvert** [2]

[1]Department of Earth, Ocean & Atmospheric Sciences Sciences, The University of British Columbia, Vancouver, Canada, [2]Department of Earth Sciences, Simon Fraser University, Vancouver, Canada

Author contributions: *Conceptualization*: Geena Littel, Michael Bostock. *Methodology*: Michael Bostock, Geena Littel, Andrew Calvert. *Formal Analysis*: Geena Littel, Michael Bostock, Charlie Sammis, Andrew Calvert. *Writing - Original draft*: Geena Littel, Michael Bostock, Charlie Sammis, Simon Peacock, Andrew Calvert.

Abstract Tremor is a weak seismic signal accompanying slow fault slip at plate boundaries. The relationship between tremor and slow slip and the tremor source mechanism have been widely debated, owing largely to the challenge of accurately locating tremor in depth. We assemble a tremor hypocenter catalog of 4,851 events in a 10×20 km^2 area beneath Vancouver Island during three slow slip episodes between 2003 and 2005 using a cross-station detection method adapted from previous studies to recover accurate depths. Improved tremor locations provide key constraints on i) thickness of the tremorgenic zone, ii) the relative location of tremor to key structural features in the subduction complex, and iii) the geologic context and mechanism of tremor. Tremor occurs in quasi-planar clusters < 500 m thick at a depth near 39 km, beneath a high reflectivity layer and within a zone of elevated Poisson's ratio with P-wave velocities of ~7 km/s. We interpret tremor as originating in the fragmentation of the upper few hundred meters of basaltic oceanic crust. Comminuted and overpressured basalt with increasingly anisotropic fabric is underplated onto overriding lithosphere to generate high reflectivity. Tremor thus manifests areas of material transfer across the plate boundary during slow slip.

Production Editor: Christie Rowe
Handling Editor: Emilie Hooft
Copy & Layout Editor: Tara Nye

Received: February 24, 2025
Accepted: July 28, 2025
Published: August 27, 2025

1 Introduction

Since the discovery of tectonic tremor in Cascadia (Rogers and Dragert, 2003), significant effort has been devoted to understanding its relation to episodic slow fault slip (i.e., episodic tremor and slip, ETS). Tectonic tremor (or simply, "tremor") is a low-amplitude seismic signal typically observed between 1–10 Hz (Obara, 2002; Katsumata and Kamaya, 2003) that usually accompanies slow slip events in Cascadia. While tremor occurs in other subduction zones and strike-slip faults worldwide (e.g., Nadeau and Dolenc, 2005; Schwartz and Rokosky, 2007; Brown et al., 2009), it is best documented in warm subduction zones, such as Cascadia and Nankai (southwest Japan). Tremor is widely regarded as a superposition of individual low-frequency earthquakes (LFEs), and it is commonly used to infer detailed migration patterns of slow slip (e.g., Ghosh et al., 2010; Rubin and Armbruster, 2013).

The source mechanism responsible for tremor has been widely debated. Contending hypotheses include: (1) shear slip in a narrow plate boundary zone, with focal mechanisms consistent with thrust faulting (Shelly et al., 2006; Ide et al., 2007; La Rocca et al., 2009; Royer and Bostock, 2014), (2) slip along multiple surfaces that are distributed across ~40 km in depth (Kao et al., 2009), (3) rapid fluid transients or pore pressure waves along the plate interface (e.g., Cruz-Atienza et al., 2018), or (4) local shear instabilities in a granular channel (Beall et al., 2019; Sammis and Bostock, 2021). Nonetheless, the sensitivity of tremor and LFE activity to Earth tides, the presence of a zone of elevated Vp/Vs, and depressed shear-wave velocity in the tremor source region imply that fluids play a significant role by lowering the effective normal stress (Audet et al., 2009; Thomas et al., 2009; Hawthorne and Rubin, 2010; Royer et al., 2015).

A primary challenge in determining the source mechanics of tremor lies in constraining its depth. Depth is difficult to measure accurately because of the low amplitudes of P-waves arising from tremor generation along shallowly or steeply dipping structures (in subduction zones or transform faults, respectively). Radiation patterns at subduction zones favor the observation of S-waves at nearby stations (e.g., Armbruster et al., 2014; Matharu et al., 2014). Therefore, most previous studies (e.g., Obara, 2002; Wech, 2010; Kao et al., 2009; Ghosh et al., 2012; Rubin and Armbruster, 2013; Bombardier et al., 2023) have used only S-waves to determine locations, frequently assuming a slab model to fix depth. Where station distributions and signal levels allow, some authors have managed to identify P-waves to better constrain depths. P-waves are occasionally visible on well isolated LFEs (e.g., Shelly et al., 2006; La Rocca et al., 2009), and accurate S–P times can also be recovered in high signal-to-noise ratio (SNR) circumstances using cross-correlation of vertical and horizontal recordings (La Rocca et al., 2009; Armbruster et al., 2014). More generally, SNRs can be improved considerably by assembling templates from hundreds of LFE detections using iterative stacking and matched-filtering to yield clear P- and S-arrivals that reveal features such as P-polarities (e.g., Royer and Bo-

*Corresponding author: bostock@mail.ubc.ca

stock, 2014) and S-wave splitting (Matharu et al., 2014; Peng et al., 2015), but with the disadvantage that only average source properties (e.g., location and focal mechanism) are characterized. Such studies have constrained LFE depths in Cascadia and Japan to depths near the inferred plate interface. However, higher precision and more systematic mapping of tremor hypocenters are required to better understand their origins. Rubin and Armbruster (2013) demonstrated how high precision tremor epicenters can be recovered from cross-station correlations of 4s duration S-wave windows at three stations. We extend this work using elements of Armbruster et al. (2014) and information on wave propagation and radiation supplied through LFE templates to improve hypocentral precision. The merit of the cross-station correlation location approach is its high relative precision that is afforded through use of a minimal number of fixed stations for which highly precise relative delay times can be determined.

Several authors have noted associations between the occurrence of tremor and underplating (i.e. material transfer from subducting to overriding plate) in warm subduction zones (Kimura et al., 2010; Bassett and Watts, 2015; Behr and Bürgmann, 2021). However, a direct link between tremor and underplating has yet to be confirmed, largely due to challenges in obtaining precise locations necessary to identify signatures of underplating. Southern Vancouver Island is the type locality for ETS (Rogers and Dragert, 2003) and provides an exceptional setting in which to address this problem because minimal crustal scattering yields comparatively clean seismic waveforms dominated by direct arrivals (e.g., Royer and Bostock (2014); cf. Plourde et al. (2015)). Moreover, stations from the temporary POLARIS array (Nicholson et al., 2005) are situated near tremor sources (see Figure 1) and are sufficiently closely spaced to yield high cross-station correlations over 4s windows for tremor during the three major ETS episodes studied here (2003, 2004, 2005) (Rubin and Armbruster, 2013; Armbruster et al., 2014; Savard and Bostock, 2015). We focus on an area well characterized by three LFE templates located near the axis of the POLARIS array, 053, 065, and 070 (as defined by Bostock et al. (2015); see Figure 1), and which has not been previously analyzed in detail. Combined with detailed seismic reflection and tomographic imaging, accurate tremor hypocenters allow us to address the relationship of tectonic tremor to subduction zone structure and underplating.

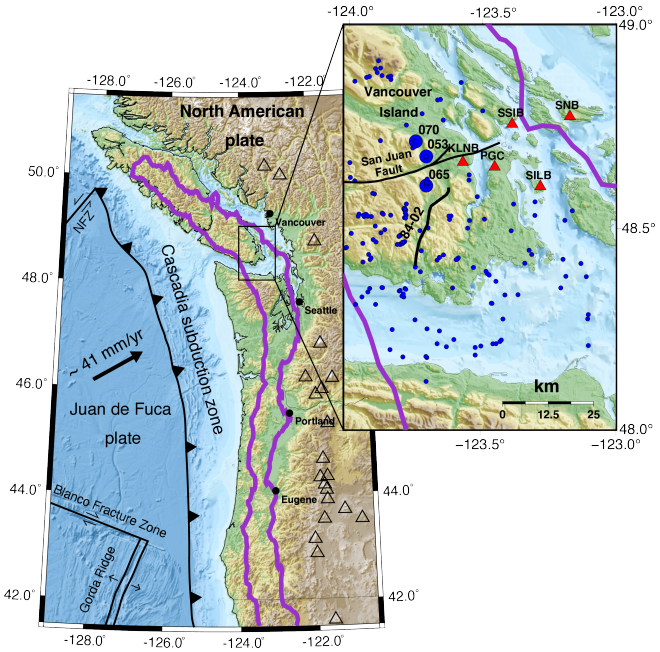

Figure 1 Map of the Cascadia region with outline of tremor epicenters from 2008–2019 (Wech, 2010) (purple line), major tectonic boundaries (black lines), and Cascade volcanoes (triangles). Map inset displays the study region. Large blue circles show the three LFE templates used in this study (065, 053, 070 from south to north); smaller blue circles are other LFE template locations (Savard et al., 2018). Red triangles are the five recording stations used in this study, and the black line is the seismic reflection profile 84-02. NFZ = Nootka Fault Zone.

2 Data and methods

We employ the P- and S-waveforms for LFE templates 053, 065, and 070 at 5 stations to determine a) delays for S- and P-wave arrivals corresponding to the nominal template location, computed using alignment procedures described in Bostock et al. (2021); b) splitting parameters that reduce the S-wave particle motions on the two horizontal coordinates to rectilinear motion isolated to a single channel (Peng et al., 2015); and c) the expected P-polarity based on clear direct P-arrivals on the vertical component of template waveforms at station SNB (Royer and Bostock, 2014); see Figure 2. These delays, splitting corrections and P-polarities derived from template waveforms, are used to normalize 24 hour-long channels for the four S-wave stations (KELB (2003)/KLNB (2004 & 2005), PGC, SILB, SSIB) and one P-wave station (SNB) employed in this study (N.B. stations KELB and KLNB differ in location by ~40 m). The S-wave stations lie close to but slightly landward of the targetted tremor region and share high SNR and strongly correlated S-waves as evidenced by the LFE templates. The choice of a suitable P-wave station is a compromise in SNR between epicentral distance and relative P-to-S radiation, as assessed from template waveforms, and is best met for the target region by station SNB (Armbruster et al., 2014).

To be more specific, we apply template-derived splitting parameters (fast-polarization direction, splitting delay) to the north and east component channels of S-wave stations to produce a single, approximately rectilinearly polarized S-wave channel for each station, taking care to ensure that each channel shares the same (positive) polarity. The same suite of station-specific splitting parameters (Table S1) is employed for all three templates to maintain the same S-wave channels for each template. We apply a multiplication factor of -1 to the SNB P-wave channel to correct the negative polarity evident on LFE templates that characterizes the shallow thrust mechanism of the LFE source excitation (Royer and Bostock, 2014). We then align these

splitting and polarity-corrected 24-hour tremor waveform channels by the relative S- and P-delay times as determined for the relevant templates (see Figure 2). PGC is designated as the time-stamp reference station (0 s delay) with the template-dependent relative shifts applied to the remaining four channels. Finally, following Rubin and Armbruster (2013), these normalized 24-hour waveforms are divided into 86,396 4s windows with 3 s overlap starting at midnight (PGC time), and cross-correlations are computed for all four pairs of S-stations with a common time stamp to maximum lags of $\pm$ 0.4 s for a given template to mitigate against cycle skips. Thus, a tremor burst originating at the nominal template epicenter will, in the absence of noise, register maximum correlation at lag (i.e. delay) $t_{ij} = 0$ s for each pair of stations i, j, whereas maximum correlations at non-zero lags characterize epicenters away from the template epicenter. The chosen maximum possible $\pm$0.4 s lag over which to search allows some overlap across the three template epicentral regions. A prospective so-called "4S" detection is declared if two conditions are met (Rubin and Armbruster, 2013) relating to thresholds on the values of a) the four possible 3-station delay-time circuits (i.e. $t_{ij} + t_{jk} - t_{ik}$, which, in the absence of errors, should equate to zero (e.g., VanDecar and Crosson, 1990)), and b) the mean cross-correlation coefficient. In the event of a 4S detection, the first principal component waveform of the aligned S-waveforms representing a high SNR version of the common signal is cross-correlated with the single-station P-waveform, and a "4S+1P" detection is declared upon meeting a second correlation coefficient threshold. The lag at maximum correlation effectively enables computation of S–P times (and therefore a hypocentral depth), and lags are again restricted to lie between $\pm$0.4 s.

The computations above are performed for two different frequency bands: a narrow band of 1.5–6 Hz like that employed by Rubin and Armbruster (2013), and a broader band of 1–8 Hz which yields fewer detections, but reduced likelihood of cycle skips due to the wider range of frequencies represented. There is, therefore, the possibility of registering up to six duplicate detections per time stamp (two frequency bands for each of the three templates). We employ thresholds, as in Rubin and Armbruster (2013), to cull the tremor catalogue to a maximum of one detection per time stamp to emphasize tremor hypocentral patterns but minimize scatter arising from false detections. We do not attempt to eliminate repeated arrivals across consecutive overlapping waveforms, thereby allowing for a continuously evolving tremor wavefield. Each detection thus represents coherent energy within 4s windows across the relevant stations. Occasionally, these windows may contain more impulsive energy corresponding to individual LFEs, but this is only infrequently the case. At the end of this processing, each 4S+1P detection is characterized by four S times and one P time, allowing for location with only one degree of redundancy (five constraints on four hypocentral parameters).

We obtain initial locations using Hypoinverse (Klein, 2002) with a 1D velocity model based on the Savard et al. (2018) 3D model at this location. After culling detections, we determine final hypocenters using double-difference relocation in tomoDD (Zhang and Thurber, 2003) with the 3D velocity model of Savard et al. (2018). We also determine accurate hypocenters for templates 053, 065 and 070 constrained using between 10 and 12 P- and 10 and 14 S-arrival time picks at 21 stations well distributed in azimuth (Royer and Bostock, 2014), with the same velocity model (Savard et al., 2018) as the tremor locations. The final 4S+1P tremor (hypocentral) catalog

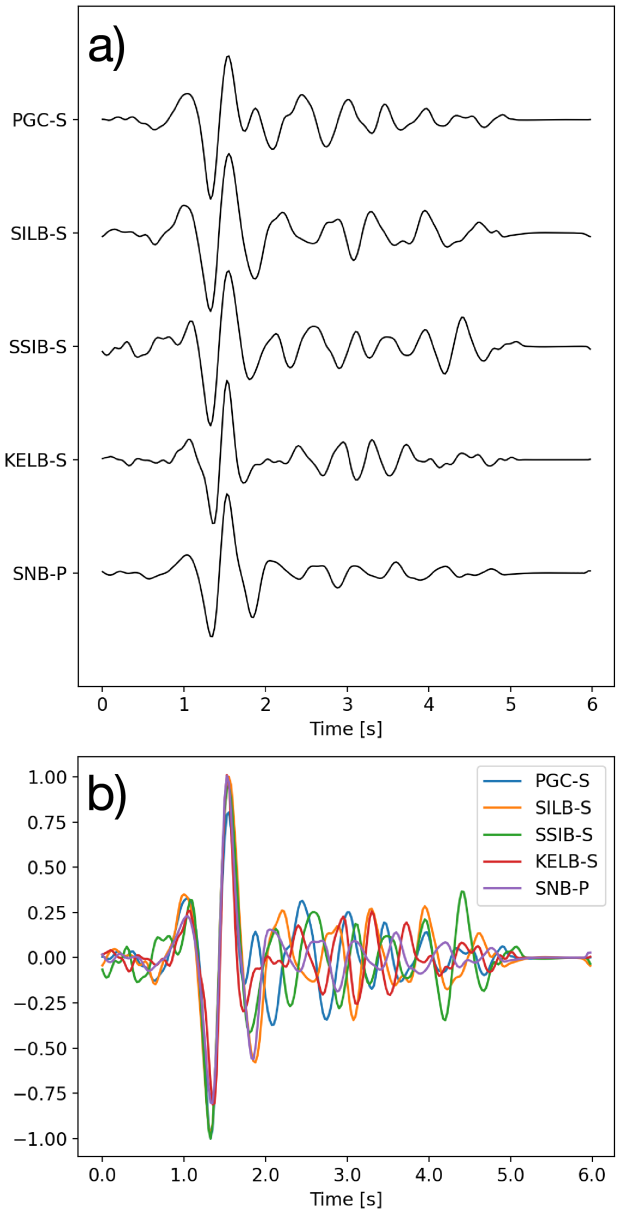

Figure 2 Example template. a) S- and P- waveforms for template 065 normalized to unit magnitude and used to locate 4s tremor windows. S-waves have been corrected for splitting and P-wave for polarity, and both have been aligned using optimal delays. These same parameters are applied to normalize 24 hr tremor seismograms prior to application of detection algorithm. Note prominence and similarity of direct arrival across channels. b) Same waveforms superposed and aligned according to optimal delays. Stations PGC, KELB/KLNB, SSIB, and SILB are used for S-wave detection, and SNB is used for P-wave detection.

represents 4,851 locations determined for a total of 13 days spread over 3 ETS episodes in 2003, 2004, and 2005. We further generate a second 4S (epicentral) tremor catalog using the S-delay times determined from the 15,986 prospective 4S detections, with epicentral locations determined using Hypoinverse and a fixed depth of 39 km; see Figure 3 and Supplement Table S2.

3 Results

3.1 Tremor Epicenters, Clusters and Patches

In map view, tremor is localized in four discrete clusters labelled 1, 2, 3, and 4 in Figure 4a. These clusters are typical of a region where tremor sources are documented to be sparsely distributed, see Armbruster et al. (2014, their figure 7), and spatially recurrent during successive slip episodes (Sammis and Bostock, 2021; Bostock et al., 2015). The template hypocenters for 053, 065 and 070 (and, in particular, their hypocentral depths) are enclosed within the three northern clusters, confirming the association between templates and individual clusters (Figure 5).

Each cluster has a different dip that we quantify using principal component analysis to define a best-fit plane to each (Table S2). We also fit one plane to all the events and two planes: one to the "northern patch" (clusters 1 and 2) and a second to the "southern patch" (clusters 3 and 4). Division into northern and southern patches was motivated by their distinct geometries in cross-section (Figure 4b), and their independent spatiotemporal rupture patterns (Figure 6a,b). Comparing the one, two, and four patch solutions, we found that two planes (northern and southern patches) best fit the data. The northern plane dips 11.2° at a 66.8° azimuth, and the southern plane dips 0.6° at a 106.9° azimuth (Figure 7). The subducting plate in this location dips at ∼11° at a ~N43°E azimuth (Bloch et al., 2023). The number of events in each cluster and its area are given in Table S2.

The distribution of distances between tremor hypocenters and the planes fit to the northern and southern patches constrains the tremor zone thickness (Figure 7). These distributions are near normal with standard deviations of 243 and 219 m, respectively, and imply that tremor observed here originates primarily within layers that are < 500 m in thickness and probably thinner considering location error (Figure 7). We note that this constraint is significantly more stringent than previous estimates, (e.g., Kao et al., 2009; Bombardier et al., 2023). Although cross-station location methods adapted from Armbruster et al. (2014) afford high relative location precision, their absolute location accuracy depends upon the accuracy of the velocity model employed in location. Accordingly, we note that the 3D velocity model of Savard et al. (2018) is the most comprehensive model compiled to date for the region. Moreover, the fact that the LFE template (053, 065, 070) hypocenters determined using P- and S-arrival time picks at $\geq$ 10 stations each and those determined using only the fixed 4S1+P station subset lie in close proximity (most notably in depth) implies that the absolute tremor locations are similarly well constrained (Figure 5). Nominal errors delivered on the (LFE template and tremor) 4S1+P hypocenters are $\pm$0.6 and $\pm$0.3 km in the horizontal and vertical directions, respectively.

3.2 Spatio-temporal patch independence

To assess the spatio-temporal behavior of epicenters, we employed the larger 4S dataset. Most of the 15,986 detections are readily associated with one of the four clusters and therefore provide a more complete measure of tremor excitation (Figures 6b, Table S2). Spatio-temporal progression of the tremor hypocenters on 16 September 2005 clearly indicates that the northern and southern patches behave independently. Similar behaviors are observed for the ETS episodes in 2003 and 2004. In Figure 6c, we display the outlines of the four clusters on a topographic map which reveals that tremor patches underlie a region of locally high topography. Moreover, the northern and southern patches are separated by a major crustal boundary and topographic low: the San Juan Fault that separates the Wrangellia and Pacific Rim (aka Leech River Schist) terranes. This observation is consistent with the results of Wells et al. (2017) who argue that tremor production is muted below major crustal faults and elevated below regions of high topography in Cascadia.

4 Discussion

Accurate determination of tremor hypocenters beneath Vancouver Island provides important constraints on their source and relation to known subduction zone structure.

4.1 Comparison of Tremor Locations with Other Observations

Constraints on subsurface structure in the study region are provided by Lithoprobe seismic reflection profiling (Clowes et al., 1987), regional double-difference tomography incorporating LFE templates (Savard et al., 2018), and receiver function studies (Audet et al., 2010; Bloch et al., 2023). Figure 8 shows tremor hypocenters from this study (green dots) overlain on a northward extrapolation of the Lithoprobe 84-02 seismic reflection profile. Panels A and B display Vp and Poisson's ratio, respectively. A dipping zone of quasi-parallel reflectors, dubbed the "E-layer" (Clowes et al., 1987), was interpreted to represent underplated imbricate oceanic sediments and volcanics. However, tomographic studies constrain the P-wave velocities at the depth of the E-layer below southern Vancouver Island to be $\geq$ 7 km/s (Figure 8; Savard et al., 2018; Calvert et al., 2020, 2011) whereas gravity modelling over the same region is consistent with high densities ranging between 2800 and 3200 kg/m^3 at comparable depths (Dehler and Clowes, 1992). Consequently, the material constituting the E-layer is most likely to be predominantly mafic in composition (Christensen, 1996). All of the E-layer, tremor and LFE template locations lie within a zone of high Poisson's ratio (~0.28) that dips landward parallel to the slab

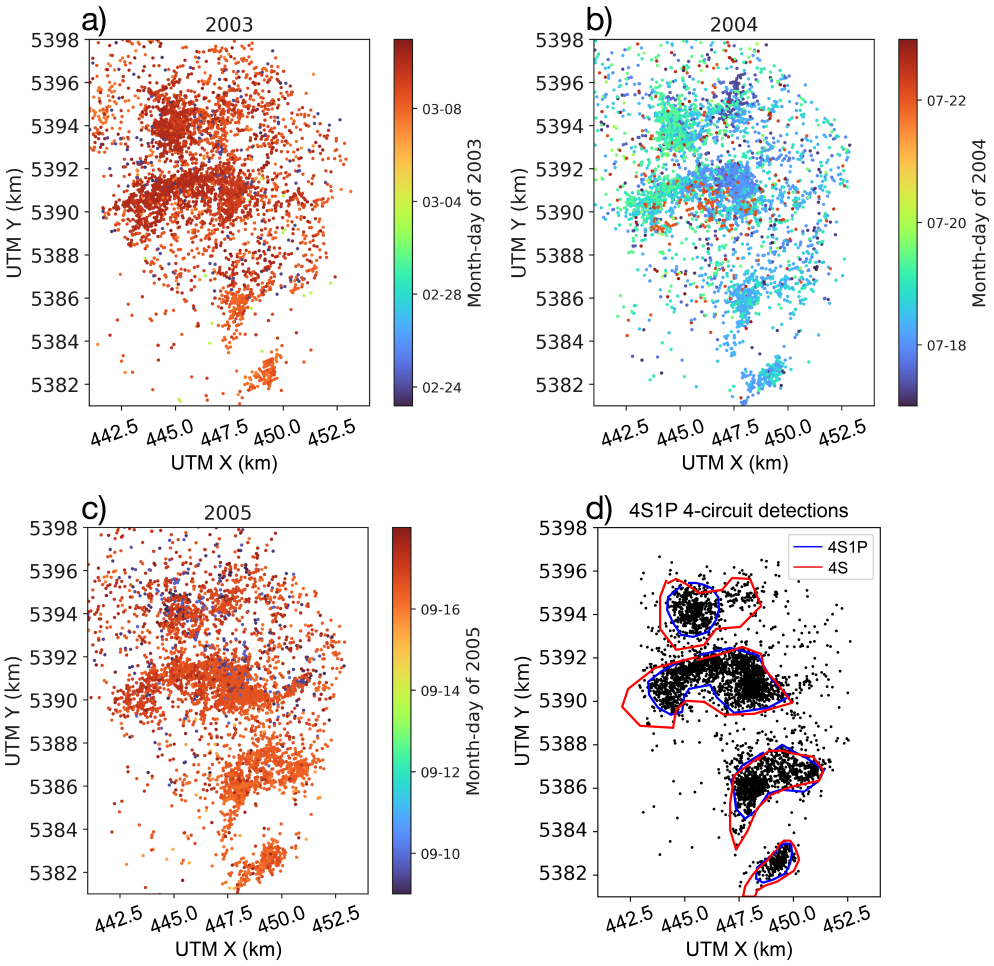

Figure 3 4S and 4S+1P catalogs. a–c) Epicenters of 15,986 4S detections for each of 3 ETS episodes in 2003, 2004, 2005, color coded with respect to time and displaying the recurrent excitation of the same 4 tremor clusters in each year. d) Epicenters for 4851 4S+1P detections including enclosing polygons employed in assembling statistics for Table S2.

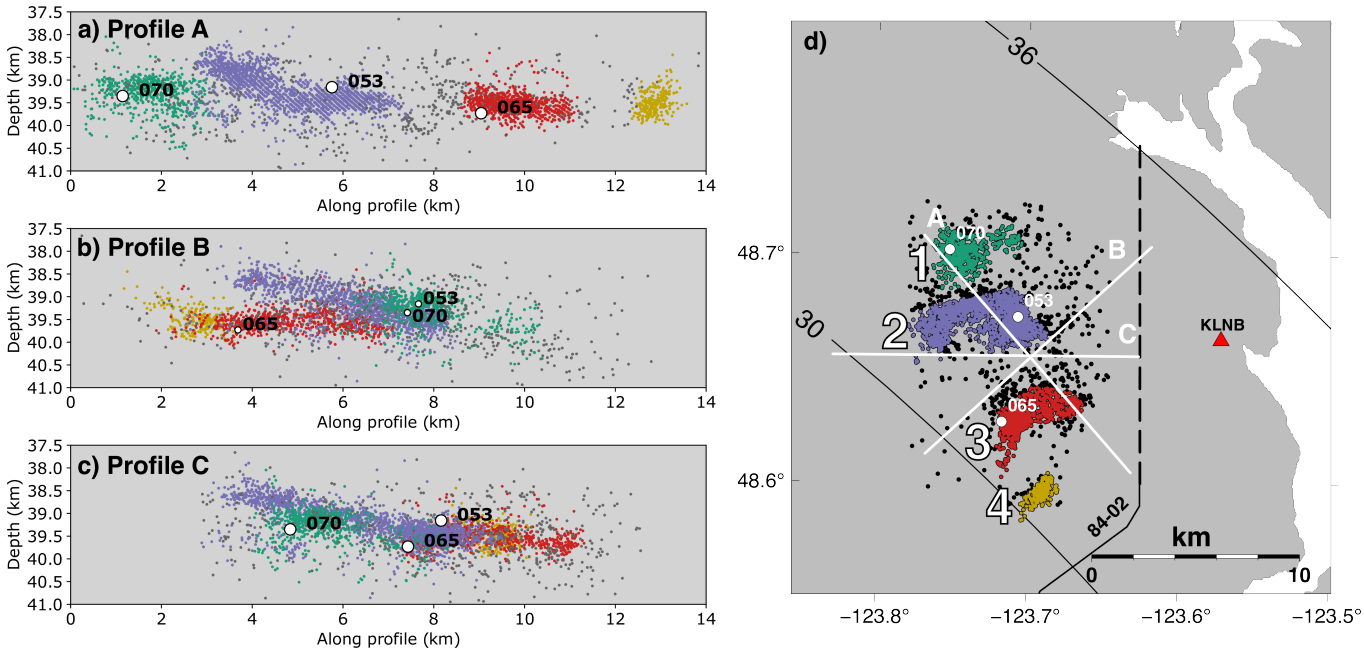

Figure 4 4S+1P hypocenters. Left panels a–c show sections of tremor hypocenters along lines A, B, and C. Hypocenters are colored by patch number. Right panel is a map view of 4,851 4S+1P epicenters during slow slip events in all three years (2003-2005). Lines A, B, and C are the profile sections to the left. White dots with number labels indicate LFE template locations. Thin black contours are top-of-plate depths of the Bloch et al. (2023) slab model.

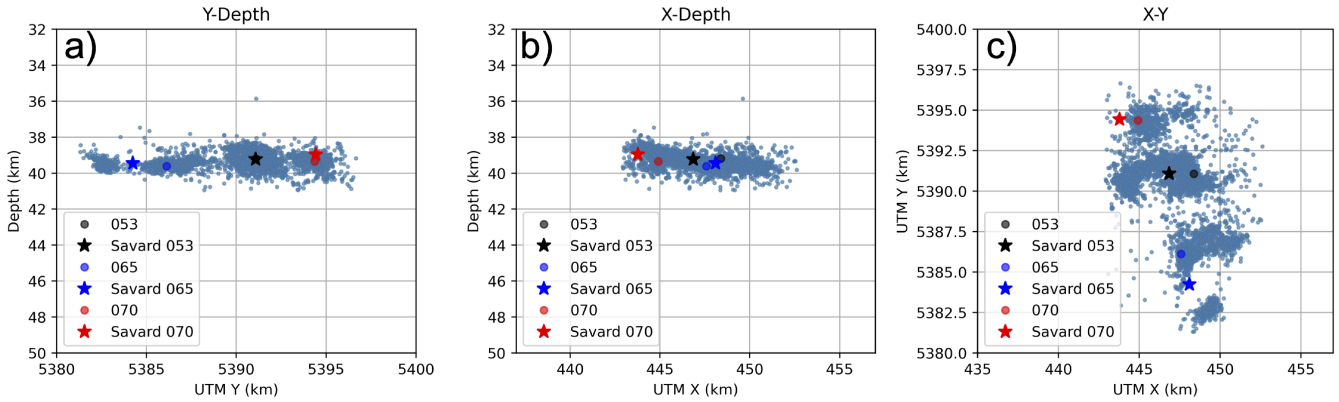

Figure 5 Depth profiles a,b) and map view c) of 4S+1P tremor locations plotted in UTM coordinates. Template (053,065,070) locations determined from processing of template waveforms using the same 4S+1P station combination are shown as colored circles, while original template locations by Savard et al. (2018) using 10–12 P- and 10–14 S-arrival time picks from 21 stations are shown as colored stars. The proximity of the two sets of template locations indicates that the absolute locations of the 4S+1P tremor hypocenters, and depth in particular, are well constrained.

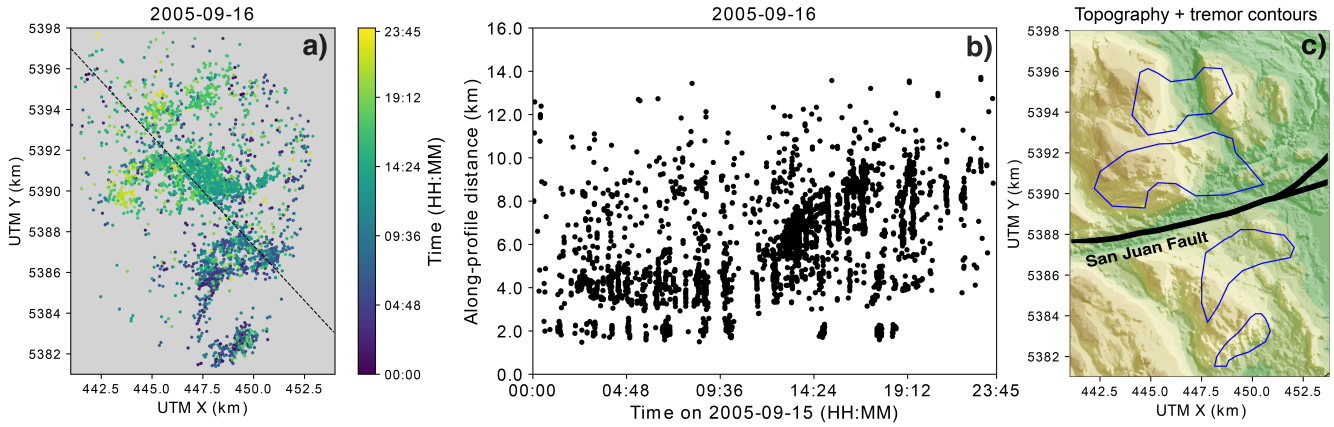

Figure 6 Temporal progression of 4S hypocenters color-coded by time on a particularly active day of the 2005 ETS episode (16 September). UTM coordinates are for zone 10U. Diagonal black dashed line in a) indicates the profile used for panel b), which shows the along-profile distance of locations for the same time-period. Note the rapid northerly migration of most events in the northern cluster as opposed to almost no migration in the southern cluster. Note also the many rapid tremor reversals which appear as near vertical streaks. c) shows the outlines of 4S hypocenters for all years, overlain on topography, with the San Juan fault. bisecting the northern patch below Wrangellia and southern patch below the Pacific Rim terrane (Leech River Schist).

and is interpreted to indicate near-lithostatic fluid pressures in the tremor source region (Audet et al., 2010; Calvert et al., 2020).

Our tremor locations indicate quasi-planar, segmented layers in the plate boundary region just below the E-layer and its northward extrapolation, at depths near 39 km and are consistent with those of nearby LFE template locations (Savard et al., 2018; Calvert et al., 2020) projected into the profile. Our observation that the E-layer lies above the locus of active tremor activity deformation (Figure 8) is contrary to reports from previous studies in this region (Kao et al., 2005; Bombardier et al., 2023). Although we cannot rule out the possibility that some tremor mapped away from the four principal patches represents true detections, most detections are tightly constrained to layers less than 500 m thick.

4.2 Tremor: Detachment and Underplating in Layer 2A

Based on our locations and information from prior structural studies, we interpret tremor beneath Vancouver Island to represent fragmentation of the top few hundreds of meters of crystalline oceanic crust (commonly referred to as layer 2A, Houtz and Ewing, 1976) of the subducting Juan de Fuca plate, as the initial stage of mafic underplating. In particular, tremor is inferred to represent shear failure associated with mixed brittle-ductile deformation within Layer 2A, which is expected to be rich in free fluids (up to ~4% by volume, Hyndman, 1988; Peacock et al., 2011) as the rocks undergo active prograde metamorphism at temperatures near 530°C and pressures of 1.1 GPa (e.g., Peacock, 2009; Gao and Wang, 2014; Angiboust et al., 2021). Meta-

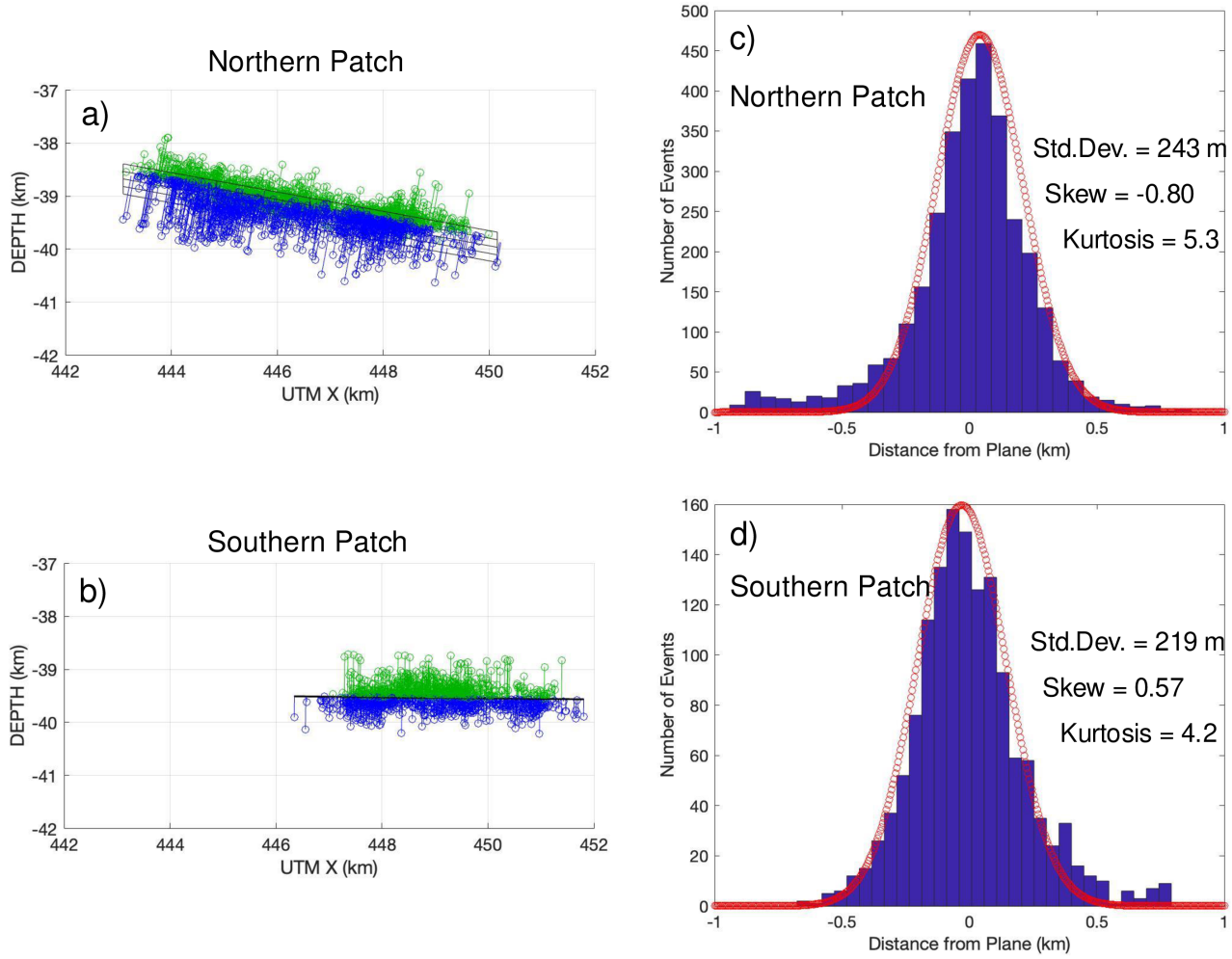

Figure 7 Plots of planar fits and normal distributions for patches 1 and 2 to justify the ± 250 m = 500 m maximum thickness of planes. Planes were fit using principal component analysis. Panels a) and b) show deviations of events from best fit plane in the northern and southern patches respectively. Red events lie above the plane, blue points below. Panels c) (northern patch) and d) (southern patch) show the distributions of distances between the planes and events. Note the distributions are nearly normal. The kurtosis of a normal distribution is 3. Observed kurtoses of 5.3 and 4.2 indicate broad tails as is evident when normal distributions (red circles) are superimposed. It is possible that the distributions are significantly narrower and that the observed standard deviations reflect, in part, uncertainty in location.

morphic fluids under these pressure-temperature conditions are under lithostatic pressure (e.g., Fyfe et al., 1978; Hyndman, 1988; Angiboust et al., 2015) and promote material weakening and localized deformation. We expect that fluid distribution within layer 2A will be heterogeneous as governed by the distribution and persistence of fault-controlled fluid pathways connecting to the seafloor prior to subduction (e.g., Fisher and Becker, 2000), thus influencing where deformation is partly brittle versus where it is purely ductile. Simple shear induced through ongoing subduction causes basaltic material to be continuously offscraped leading to comminuted wear products with an increasingly anisotropic fabric that are gradually plated onto the overriding lithosphere. Weaker volumes with higher water contents trapped by a highly anisotropic permeability are elongated by ductile shear to produce the seismic reflectors that characterize the E-layer (Calvert and Clowes, 1990; Hyndman, 1988; Nedimović et al., 2003), which is mostly aseismic (e.g., Figure 8). We emphasize that in this interpretation, deformation within the E-layer is ductile and continuing (e.g., Roy et al., 2021), contrasting with interpretations that involve E-layer assembly through a series of ancient and sequential thrust faults producing duplex structures (Calvert, 2004; Angiboust et al., 2021). Localized areas where material transfer is initiating within the subduction zone thus manifest as the distinct tremor patches in Figure 4; see also Sweet et al. (2019).

4.3 Olympic Peninsula Test

To test this interpretation, we consider geophysical data from the Olympic Peninsula in Washington state. This location is the only one in Cascadia away from Vancouver Island where all three of a) a high-resolution seismic reflection profile (SHIPS, e.g., Calvert et al., 2003), b) highly resolved 3D body wave Vp and Vs tomography models (Merrill et al., 2020), and c) a high density of seis-

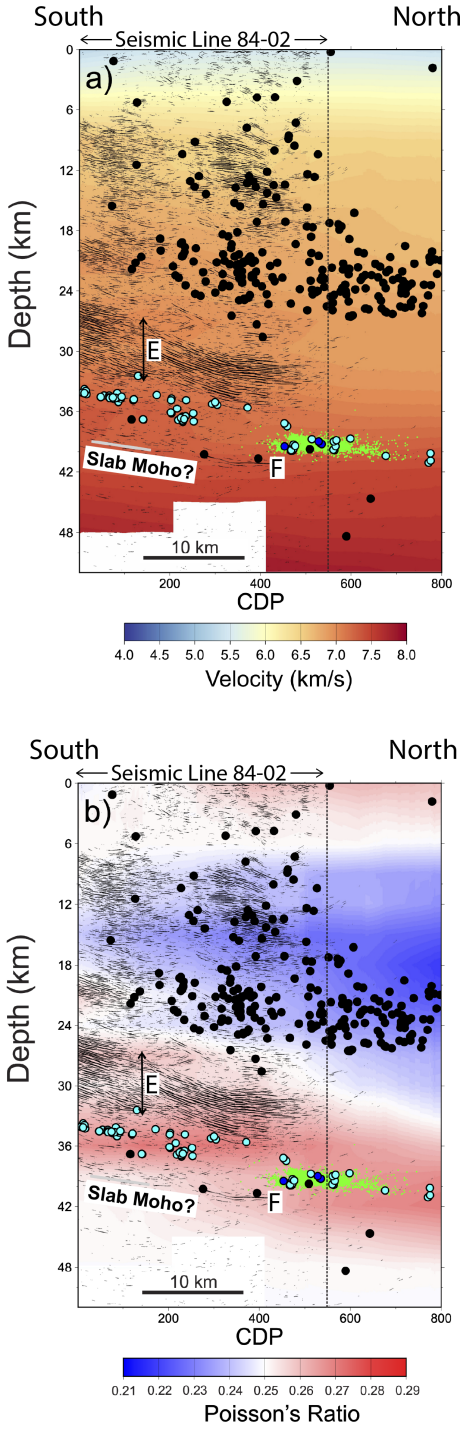

Figure 8 Depth section of tremor (green dots) overlain on a) P-wave velocity and b) Poisson's ratio (Savard et al., 2018) and the seismic reflection profile 84-02 (Clowes et al., 1987), modified from Calvert et al. (2020). Horizontal distance is defined by Common Depth Point (CDP). LFE template locations from Savard et al. (2018) are in light blue circles, 4S+1P template 053, 065, 070 locations are in dark blue circles, and forearc crustal seismicity are in black circles. Grey line is a wide-angle reflector interpreted by Preston et al. (2003) to represent the oceanic Moho. The labels E and F denote the E-layer and the oceanic Moho, respectively, as originally interpreted by Clowes et al. (1987).

mic instruments capable of highly resolving tremor and LFEs (Ghosh et al., 2012; Peng and Rubin, 2016), overlap sufficiently to examine the geologic context of tremor. The Olympic Peninsula is widely recognized to be composed of and underlain by thick sequences of sediments that were underplated by and likely extend down to, the subducting plate (Brandon et al., 1998; Calvert et al., 2011). The geological context is therefore distinct from the overriding plate on Vancouver Island and provides a strong independent test of the tremor origin model we propose.

We use tremor epicenter (Peng et al., 2015) and LFE (Savard et al., 2018) catalogs to assemble an updated suite of LFE templates where tremor and the SHIPS JDF-2 reflection profile intersect (Figure 9). Locations for these templates are constrained by 15–40 P- and S-wave times from both sides of the Strait of Juan de Fuca and computed using the same velocity model (Merrill et al., 2020) used to migrate reflection data along the depth profile. The key result is that the LFE templates are located in a material with Vp ~7km/s, which is below a lower velocity (Vp ~6.5 km/s), ~10 km thick, high reflectivity E-layer. The location of the templates is consistent with the occurrence of tremor and a detachment horizon within layer 2A. Moreover, both the increased E-layer thickness and its lower velocity of 6.5 km/s midway between metagreywackes and metabasalt (Christensen, 1996) indicate that, unlike Vancouver Island, underplating here has involved a mixture of crystalline oceanic basement and overlying oceanic sediments.

4.4 Additional Support for Tremor – Underplating Association

Additional support from other geoscientific data for the tremor-mafic underplating model is multifold. Based on analyses of multiple exhumed accretionary complexes, Kimura and Ludden (1995) argued that exhumed, underplated basalt occurs as thin (mean thickness 80–100 m) layers derived exclusively from layer 2A. In the geologic record, mafic schists are a common component of underplated material recovered from 15–50 km depth in paleo ocean-continent subduction zones (e.g., Angiboust et al., 2021, and references therein). Moreover, the coherent, coast-parallel distributions of tremor epicenters along both Cascadia (Wech, 2010) and other warm subduction forearcs (e.g., Obara, 2002; Gallego et al., 2013) seem unlikely were tremor associated with sediments, given the variable sediment inputs and subduction styles along these margins. As previously noted by Bassett and Watts (2015); Brudzinski and Allen (2007) and Wells et al. (2017), tremor epicentral distributions and densities also generally mirror the high coastal topography associated with warm subduction zone settings. Brudzinski and Allen (2007) also noted that ETS recurrence intervals are inversely correlated with topography. Moreover, this topography is well modelled as due to underplating processes (Angiboust et al., 2021; Menant et al., 2019). Collectively, this wide array of observations supports the thesis that tectonic tremor in subduction zones is associated with underplating at a detachment horizon

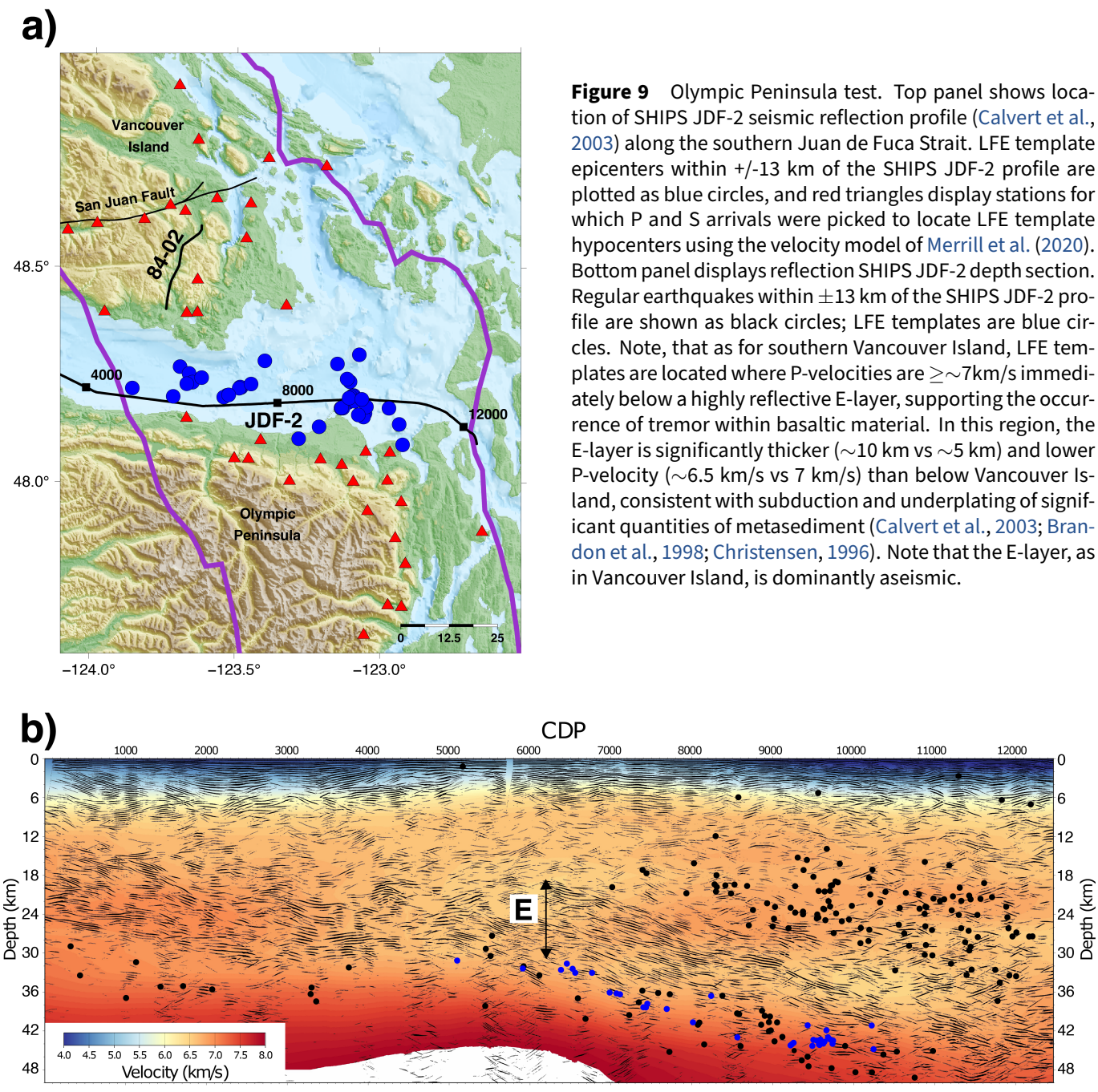

Figure 9 Olympic Peninsula test. Top panel shows location of SHIPS JDF-2 seismic reflection profile (Calvert et al., 2003) along the southern Juan de Fuca Strait. LFE template epicenters within +/-13 km of the SHIPS JDF-2 profile are plotted as blue circles, and red triangles display stations for which P and S arrivals were picked to locate LFE template hypocenters using the velocity model of Merrill et al. (2020). Bottom panel displays reflection SHIPS JDF-2 depth section. Regular earthquakes within $\pm$13 km of the SHIPS JDF-2 profile are shown as black circles; LFE templates are blue circles. Note, that as for southern Vancouver Island, LFE templates are located where P-velocities are $\geq\sim$7km/s immediately below a highly reflective E-layer, supporting the occurrence of tremor within basaltic material. In this region, the E-layer is significantly thicker ($\sim$10 km vs $\sim$5 km) and lower P-velocity ($\sim$6.5 km/s vs 7 km/s) than below Vancouver Island, consistent with subduction and underplating of significant quantities of metasediment (Calvert et al., 2003; Brandon et al., 1998; Christensen, 1996). Note that the E-layer, as in Vancouver Island, is dominantly aseismic.

within layer 2A.

4.5 Granular Jamming and Underplating

Although Kimura and Ludden (1995) suggested a "peeling" of layer 2A in the transfer of metabasalt from subducting to overriding plates, the nature of tremor suggests an origin involving significant cataclasis (Kirkpatrick et al., 2021; Oncken et al., 2021). For example, Sammis and Bostock (2021) documented lognormal distributions of LFE moments that that they argue can be explained via a model for tremor generation caused by shear failure at contacts between rigid grains jammed (and producing stress bridges) within a viscous channel. The granular jamming concept can be viewed as a special instance of "asperity-in-matrix" models that have achieved success in simulating various aspects of ETS phenomenology (Luo and Ampuero, 2014, 2018; Luo and Liu, 2019, 2021) and consider tremor to be generated at localized "asperities" distinct from slow slip that occurs in an enveloping ductile "matrix". To further test this idea, we estimated the scalar moment and moment magnitude for each tremor detection using an energy proxy following Rubin and Armbruster (2013) and calibrated to the LFE moment catalog of Bostock et al. (2015). Specifically, we assign a consistent, coherent radiated energy metric for each 4s, narrow-band S-detection window as

$$E(t) = \frac{S_A(t)S_B(t'_B) + S_A(t)S_C(t'_C) + S_B(t'_B)S_C(t'_C)}{3},$$

where $S(t)$ is the S-wave seismogram, A, B, C denote stations PGC, SILB, SSIB, respectively, and t' is the time offset between the tremor arrival at stations B or C and PGC. To assign magnitudes from energy, we identify those 4s windows (a total of 391) that correspond to

matched filtered LFE detections with magnitudes from the catalog of Bostock et al. (2015) and perform a power-law regression between LFE moment and tremor energy for detections common to both catalogs to establish the following calibration for moment magnitude:

$$M_W = 0.238 \log_{10}(E) + 0.319,$$

yielding the scalar moments for all available S-wave windows as

$$M_0 = 10^{(1.5 M_W + 10.7)}.$$

Histograms of M_W and M_0 are displayed in Figure 10. As in Sammis and Bostock (2021), we observe a narrow normal distribution of magnitudes ($M_W = 1.60 \pm 0.1$), implying a lognormal distribution of scalar moments. Total moment released in each of the four clusters is given in Table S2. We will assume that these lognormal distributions are not significantly influenced by catalog incompleteness. Although Sammis and Bostock (2021) were not able to definitively exclude the possibility of detection bias, they did provide evidence supporting catalog completeness based on independent observations of Supino et al. (2020, 2021) and minor differences in nighttime versus daytime detections (see section 2.3 of Sammis and Bostock, 2021).

Thus, in the current context, we interpret the granular (i.e. asperity) and viscous (i.e. matrix) elements of layer 2A to be associated with less altered tracts of metabasalt surrounded by a more intensely hydrated and overpressured matrix, respectively, and involving slip surfaces of order 100 m in dimension (Sammis and Bostock, 2021). The lognormal distribution of moments originates from the lognormal distribution of contact areas within granular jams expected as larger competent clasts are gradually broken down into smaller ones. As the clasts decrease in size, they become less prone to jamming, and we suggest that a scale-dependence set by layer 2A thickness is responsible for the apparent band-limitation (~1–10 Hz) of tremor (e.g., Obara, 2002), and the limited range of magnitudes and tremor energies observed in Sammis and Bostock (2021) and in this paper, respectively.

As comminution proceeds, we expect increasing shear strain, ductile deformation, and gradual material transfer/transformation to the E-layer because of decreased density and strength imparted by the release of fluids (Gerya and Meilick, 2010; Menant et al., 2020). The dominant rock types manifested in this process would be foliated cataclasites transitioning to mylonites, as has been documented for the inferred plate boundary of the Central Alps suture zone (Oncken et al., 2021). We note that tremor and LFE template hypocenters lie on average 2–3 km below the base of the reflectivity that defines the E-layer in Figure 5. We discount the possibility of significant location bias since the same velocity model (Savard et al., 2018) is used to locate hypocenters and migrate reflections (Figure 8), and the three northern cluster locations enclose the respective template locations (Figure 5). Rather, we argue that, at some point in the comminution and shearing process, a permeability anisotropy "percolation" threshold is reached wherein fluids become segregated

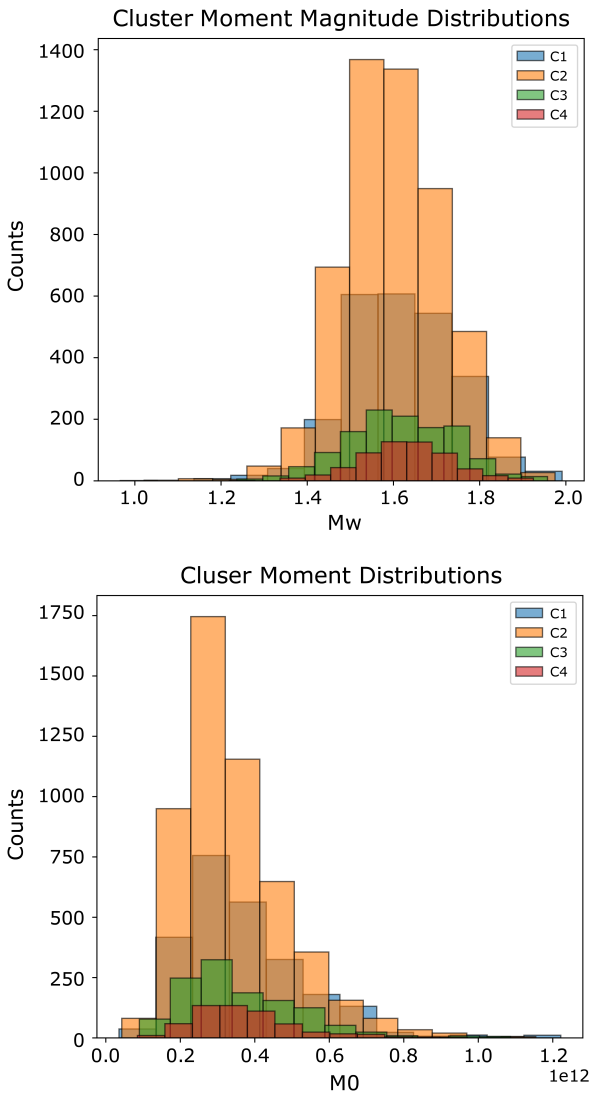

Figure 10 Histogram distributions of a) moment magnitude, M_W, and b) scalar moment, M_0, for each cluster. Magnitude distributions are approximately normal meaning that moment distributions are approximately lognormal.

within horizontally contiguous "lenses" producing the pronounced reflectivity horizons and abrupt base that define the E-layer, perhaps through changes in dihedral angle as suggested by Hyndman (1988). Although the estimates of slip within tremorgenic volumes based on Kostrov strain made by Sammis and Bostock (2021) significantly exceed those previously reported for tremor within the ETS zone more generally (Kao et al., 2010), they nonetheless fall far short of the plate motion budget (~3 mm versus ~4 cm per ETS episode) indicating that (macroscopically) ductile deformation must still dominate. It is likely then that the slow slip of ETS represents ductile shear persisting into the E-layer, both where tremor is well expressed and where it is not (e.g., Wech and Bartlow, 2014). The sparse distribution of tremor sources over the broader region when imaged at high resolution (see Armbruster et al., 2014, their Figure 7) suggests that the large areas of fault zone

surrounding tremorgenic patches are aseismic because creep in those areas is not (currently) inhibited by stuck asperities (i.e. granular jams / stress bridges) associated with initiation of material transfer.

4.6 Mass Balance in Formation of the E-layer

We assess the feasibility of E-layer assembly over realistic time periods using mass balance calculations modified from Clowes et al. (1987). We assume the E-layer has a downdip length of 100 km and is 5 km thick beneath Vancouver Island, corresponding to a volume of 500 km^3/km along strike. Roughly 1800 km of plate have been subducted beneath Vancouver Island over the last 40 Ma(Clowes et al., 1987, see their table 2). If a thickness H of the basalt layer was offscraped during this time to form the E-layer, the underplated volume is $1800\,H$ km^3/km along strike. If the E-layer was formed through basal accretion of layer 2A, then $1800\,H = 500$, or $H = 280$ m, in rough agreement with the thickness of the layer 2A pillow basalts (Houtz and Ewing, 1976; Houtz, 1976). Moreover, the total relative displacement of the Juan de Fuca Plate and the thickness of the E-layer are consistent with an extrapolation of the observed relation between displacement and thickness of crustal fault zones (Figure 11, Scholz, 1987; Hull, 1988). A doubling in thickness of the E-layer to ~10 km (and decrease in associated Vp to ~6.5 km/s) below the Olympic Peninsula likely reflects the underplating of a comparable proportion of sediment overlying layer 2A wherein detachment takes place.

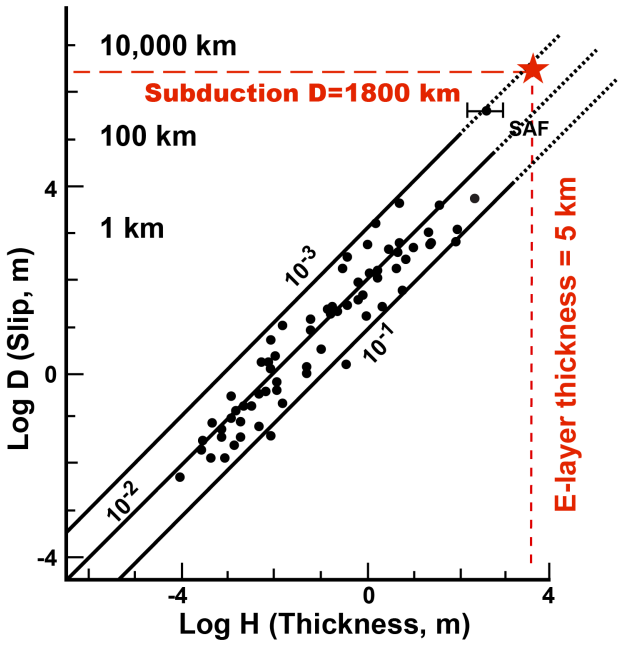

Figure 11 Log-log plot of gouge thickness H as a function of total slip D redrawn from Scholz (1987). Point SAF was estimated by Scholz for the San Andreas fault in central California and was confirmed by SAFOD drill core. The line is extended to the slip and E-layer thickness appropriate for subduction beneath Vancouver Island (Figure 8, Clowes et al., 1987).

5 Conclusions

Our study of tectonic tremor hypocenters originating within a 10×20 km^2 area below Vancouver Island has led to the following observations, interpretations, and conclusions:

1) Tremor occurs in two patches of two clusters each, where each patch is quasi-planar in aspect and possesses a distinct geometry and rupture history. Moreover, each cluster is spatially recurrent over three consecutive ETS episodes.

2) The patches are no thicker than 500 m and probably thinner.

3) Both patches and previously located LFE template hypocenters reside several km below the E-layer, a 5 km thick highly reflective shear zone, and within a volume characterized by elastic wave velocities and density that imply a basaltic composition and high pore pressures.

4) Tremor magnitude proxies are consistent with a previous study of LFE moments that advocates an asperity-in-matrix granular jamming model for tremor genesis.

5) These observations lead to a plausible geologic context for tremor genesis involving localized disaggregation of a metamorphosed, overpressured layer 2A of the subducting plate, followed by underplating and eventual incorporation of layer 2A material within the E-layer.

6) This hypothesis is supported by complementary geophysical observations below the northern Olympic Peninsula, geologic studies of exhumed oceanic crust, associations of Cascadia ETS recurrence intervals and tremor intensity with forearc topography, tremor distributions in other warm subduction forearcs, and geodynamic modelling of forearc topography.

7) We note the additional occurrence of tectonic tremor beneath accretionary prisms in subduction zones such as Nankai (Obana and Kodaira, 2009), where material transfer is also implied, and at major strike-slip faults, such as the Alpine (Wech et al., 2012) and San Andreas Faults (Nadeau and Dolenc, 2005). We suggest that the occurrence of tremor in these environments, as in the deep plate boundary of warm subduction zones, may be diagnostic of granular comminution and flow and/or material transfer in zones of high pore-fluid pressure (e.g., Saffer and Tobin, 2011; Beroza and Ide, 2011).

Acknowledgements

We are grateful for the constructive reviews supplied by two anonymous reviewers and editor Emilie Hooft that led to significant improvements in the manuscript. This work was supported through Natural Sciences and Engineering Research Council of Canada Discovery grants RGPIN-2021-03039, RGPIN-2020-07066 and RGPIN-2023-3377 to M.G.B, S.M.P and A.J.C., respectively.

Data and code availability

The final detection catalogs can be accessed on the figshare repository with the following URL:

https://doi.org/10.6084/m9.figshare.c.7947842.v1. Waveforms for the permanent CNSN network and POLARIS temporary array can be obtained from the Earthquakes Canada (Natural Resources Canada) database (https://earthquakescanada.nrcan.gc.ca). The hypoDD software is available for download from: https://www.ldeo.columbia.edu/~felixw/hypoDD.html and tomoDD is available from Clifford Thurber. Hypoinverse is available from: https://www.usgs.gov/software/hypoinverse-earthquake-location. Migrated seismic reflection data and coordinates of line 84-02 are available in SEGY format from the archive of the Geological Survey of Canada (https://open.canada.ca/data/en/dataset/f96393c4-29c7-5624-80cd-046a1496b4c0). Most figures were produced using the Generic Mapping Tools package [79].

Codes (in Python) used to generate the tremor detection catalog are provided in the figshare repository with the same URL.

Competing interests

The authors declare no competing interests, financial or otherwise

References

Angiboust, S., Kirsch, J., Oncken, O., Glodny, J., Monié, P., and Rybacki, E. Probing the transition between seismically coupled and decoupled segments along an ancient subduction interface. *Geochemistry, Geophysics, Geosystems*, 16(6):1905–1922, June 2015. doi: 10.1002/2015gc005776.

Angiboust, S., Menant, A., Gerya, T., and Oncken, O. The rise and demise of deep accretionary wedges: A long-term field and numerical modeling perspective. *Geosphere*, 18(1):69–103, Nov. 2021. doi: 10.1130/ges02392.1.

Armbruster, J. G., Kim, W., and Rubin, A. M. Accurate tremor locations from coherent S and P waves. *Journal of Geophysical Research: Solid Earth*, 119(6):5000–5013, June 2014. doi: 10.1002/2014jb011133.

Audet, P., Bostock, M. G., Christensen, N. I., and Peacock, S. M. Seismic evidence for overpressured subducted oceanic crust and megathrust fault sealing. *Nature*, 457(7225):76–78, Jan. 2009. doi: 10.1038/nature07650.

Audet, P., Bostock, M. G., Boyarko, D. C., Brudzinski, M. R., and Allen, R. M. Slab morphology in the Cascadia fore arc and its relation to episodic tremor and slip. *Journal of Geophysical Research: Solid Earth*, 115(B4), Apr. 2010. doi: 10.1029/2008jb006053.

Bassett, D. and Watts, A. B. Gravity anomalies, crustal structure, and seismicity at subduction zones: 2. Interrelationships between fore-arc structure and seismogenic behavior. *Geochemistry, Geophysics, Geosystems*, 16(5):1541–1576, May 2015. doi: 10.1002/2014gc005685.

Beall, A., Fagereng, Å and Ellis, S. Strength of Strained Two-Phase Mixtures: Application to Rapid Creep and Stress Amplification in Subduction Zone Mélange. *Geophysical Research Letters*, 46 (1):169–178, Jan. 2019. doi: 10.1029/2018gl081252.

Behr, W. M. and Bürgmann, R. What's down there? The structures, materials and environment of deep-seated slow slip and tremor. *Philosophical Transactions of the Royal Society A: Mathematical, Physical and Engineering Sciences*, 379(2193): 20200218, Feb. 2021. doi: 10.1098/rsta.2020.0218.

Beroza, G. C. and Ide, S. Slow Earthquakes and Nonvolcanic Tremor. *Annual Review of Earth and Planetary Sciences*, 39 (1):271–296, May 2011. doi: 10.1146/annurev-earth-040809-152531.

Bloch, W., Bostock, M. G., and Audet, P. A Cascadia Slab Model From Receiver Functions. *Geochemistry, Geophysics, Geosystems*, 24(10), Oct. 2023. doi: 10.1029/2023gc011088.

Bombardier, M., Dosso, S. E., Cassidy, J. F., and Kao, H. Tackling the challenges of tectonic tremor localization using differential traveltimes and Bayesian inversion. *Geophysical Journal International*, 234(1):479–493, Feb. 2023. doi: 10.1093/gji/ggad086.

Bostock, M., Plourde, A., Drolet, D., and Littel, G. Multichannel Alignment of S Waves. *Bulletin of the Seismological Society of America*, 112(1):133–142, Sept. 2021. doi: 10.1785/0120210076.

Bostock, M. G., Thomas, A. M., Savard, G., Chuang, L., and Rubin, A. M. Magnitudes and moment-duration scaling of low-frequency earthquakes beneath southern Vancouver Island. *Journal of Geophysical Research: Solid Earth*, 120(9):6329–6350, Sept. 2015. doi: 10.1002/2015jb012195.

Brandon, M. T., Roden-Tice, M. K., and Garver, J. I. Late Cenozoic exhumation of the Cascadia accretionary wedge in the Olympic Mountains, northwest Washington State. *Geological Society of America Bulletin*, 110(8):985–1009, 1998. doi: 10.1130/0016-7606(1998)110<0985:LCEOTC>2.3.CO;2.

Brown, J. R., Beroza, G. C., Ide, S., Ohta, K., Shelly, D. R., Schwartz, S. Y., Rabbel, W., Thorwart, M., and Kao, H. Deep low-frequency earthquakes in tremor localize to the plate interface in multiple subduction zones. *Geophysical Research Letters*, 36(19), Oct. 2009. doi: 10.1029/2009gl040027.

Brudzinski, M. R. and Allen, R. M. Segmentation in episodic tremor and slip all along Cascadia. *Geology*, 35(10):907, 2007. doi: 10.1130/g23740a.1.

Calvert, A. and Clowes, R. Deep, high-amplitude reflections from a major shear zone above the subducting Juan de Fuca plate. *Geology*, 18(11):1091–1094, 1990. doi: 0.1130/0091-7613(1990)018<1091:DHARFA>2.3.CO;2.

Calvert, A. J. Seismic reflection imaging of two megathrust shear zones in the northern Cascadia subduction zone. *Nature*, 428 (6979):163–167, Mar. 2004. doi: 10.1038/nature02372.

Calvert, A. J., Fisher, M. A., Ramachandran, K., and Tréhu, A. M. Possible emplacement of crustal rocks into the forearc mantle of the Cascadia Subduction Zone. *Geophysical Research Letters*, 30(23), Dec. 2003. doi: 10.1029/2003gl018541.

Calvert, A. J., Preston, L. A., and Farahbod, A. M. Sedimentary underplating at the Cascadia mantle-wedge corner revealed by seismic imaging. *Nature Geoscience*, 4(8):545–548, July 2011. doi: 10.1038/ngeo1195.

Calvert, A. J., Bostock, M. G., Savard, G., and Unsworth, M. J. Cascadia low frequency earthquakes at the base of an overpressured subduction shear zone. *Nature Communications*, 11(1), Aug. 2020. doi: 10.1038/s41467-020-17609-3.

Christensen, N. I. Poisson's ratio and crustal seismology. *Journal of Geophysical Research: Solid Earth*, 101(B2):3139–3156, Feb. 1996. doi: 10.1029/95jb03446.

Clowes, R. M., Brandon, M. T., Green, A. G., Yorath, C. J., Brown, A. S., Kanasewich, E. R., and Spencer, C. LITHOPROBE—southern Vancouver Island: Cenozoic subduction complex imaged by deep seismic reflections. *Canadian Journal of Earth Sciences*, 24 (1):31–51, Jan. 1987. doi: 10.1139/e87-004.

Cruz-Atienza, V. M., Villafuerte, C., and Bhat, H. S. Rapid tremor migration and pore-pressure waves in subduction zones. *Nature Communications*, 9(1), July 2018. doi: 10.1038/s41467-018-05150-3.

Dehler, S. A. and Clowes, R. M. Integrated geophysical modelling of terranes and other structural features along the western Canadian margin. *Canadian Journal of Earth Sciences*, 29 (7):1492–1508, July 1992. doi: 10.1139/e92-119.

Fisher, A. T. and Becker, K. Channelized fluid flow in oceanic crust reconciles heat-flow and permeability data. *Nature*, 403(6765): 71–74, Jan. 2000. doi: 10.1038/47463.

Fyfe, W. S., Price, N. J., and Thompson, A. B. *Fluids in the Earth's Crust: Their Significance in Metamorphic, Tectonic, and Chemical Transport Processes*, volume 1 of *Developments in Geochemistry*. Elsevier Scientific Publishing Company, 1978. https://books.google.fr/books?id=b-cJAQAAIAAJ.

Gallego, A., Russo, R. M., Comte, D., Mocanu, V., Murdie, R. E., and VanDecar, J. Tidal modulation of continuous nonvolcanic seismic tremor in the Chile triple junction region. *Geochemistry, Geophysics, Geosystems*, 14(4):851–863, Apr. 2013. doi: 10.1002/ggge.20091.

Gao, X. and Wang, K. Strength of stick-slip and creeping subduction megathrusts from heat flow observations. *Science*, 345 (6200):1038–1041, Aug. 2014. doi: 10.1126/science.1255487.

Gerya, T. V. and Meilick, F. I. Geodynamic regimes of subduction under an active margin: effects of rheological weakening by fluids and melts. *Journal of Metamorphic Geology*, 29(1):7–31, Oct. 2010. doi: 10.1111/j.1525-1314.2010.00904.x.

Ghosh, A., Vidale, J. E., Sweet, J. R., Creager, K. C., Wech, A. G., Houston, H., and Brodsky, E. E. Rapid, continuous streaking of tremor in Cascadia. *Geochemistry, Geophysics, Geosystems*, 11 (12), Dec. 2010. doi: 10.1029/2010gc003305.

Ghosh, A., Vidale, J. E., and Creager, K. C. Tremor asperities in the transition zone control evolution of slow earthquakes. *Journal of Geophysical Research: Solid Earth*, 117(B10), Oct. 2012. doi: 10.1029/2012jb009249.

Hawthorne, J. C. and Rubin, A. M. Tidal modulation of slow slip in Cascadia. *Journal of Geophysical Research: Solid Earth*, 115(B9), Sept. 2010. doi: 10.1029/2010jb007502.

Houtz, R. and Ewing, J. Upper crustal structure as a function of plate age. *Journal of Geophysical Research*, 81(14):2490–2498, May 1976. doi: 10.1029/jb081i014p02490.

Houtz, R. E. Seismic properties of layer 2A in the Pacific. *Journal of Geophysical Research*, 81(35):6321–6331, Dec. 1976. doi: 10.1029/jb081i035p06321.

Hull, J. Thickness-displacement relationships for deformation zones. *Journal of Structural Geology*, 10(4):431–435, Jan. 1988. doi: 10.1016/0191-8141(88)90020-x.

Hyndman, R. D. Dipping Seismic Reflectors, Electrically Conductive Zones, and Trapped Water in the Crust Over a Subducting Plate. *Journal of Geophysical Research: Solid Earth*, 93(B11): 13391–13405, Nov. 1988. doi: 10.1029/jb093ib11p13391.

Ide, S., Shelly, D. R., and Beroza, G. C. Mechanism of deep low frequency earthquakes: Further evidence that deep nonvolcanic tremor is generated by shear slip on the plate interface. *Geophysical Research Letters*, 34(3), Feb. 2007. doi: 10.1029/2006gl028890.

Kao, H., Shan, S.-J., Dragert, H., Rogers, G., Cassidy, J. F., and Ramachandran, K. A wide depth distribution of seismic tremors along the northern Cascadia margin. *Nature*, 436(7052): 841–844, Aug. 2005. doi: 10.1038/nature03903.

Kao, H., Shan, S., Dragert, H., and Rogers, G. Northern Cascadia episodic tremor and slip: A decade of tremor observations from 1997 to 2007. *Journal of Geophysical Research: Solid Earth*, 114 (B11), Nov. 2009. doi: 10.1029/2008jb006046.

Kao, H., Wang, K., Dragert, H., Kao, J. Y., and Rogers, G. Estimating seismic moment magnitude (Mw) of tremor bursts in northern Cascadia: Implications for the "seismic efficiency" of episodic tremor and slip. *Geophysical Research Letters*, 37(19), Oct. 2010. doi: 10.1029/2010gl044927.

Katsumata, A. and Kamaya, N. Low-frequency continuous tremor around the Moho discontinuity away from volcanoes in the southwest Japan. *Geophysical Research Letters*, 30(1), Jan. 2003. doi: 10.1029/2002gl015981.

Kimura, G. and Ludden, J. Peeling oceanic crust in subduction zones. *Geology*, 23(3):217–220, 1995. doi: 10.1130/0091-7613(1995)023<0217:POCISZ>2.3.CO;2.

Kimura, H., Takeda, T., Obara, K., and Kasahara, K. Seismic Evidence for Active Underplating Below the Megathrust Earthquake Zone in Japan. *Science*, 329(5988):210–212, July 2010. doi: 10.1126/science.1187115.

Kirkpatrick, J. D., Fagereng, Å and Shelly, D. R. Geological constraints on the mechanisms of slow earthquakes. *Nature Reviews Earth & Environment*, 2(4):285–301, Mar. 2021. doi: 10.1038/s43017-021-00148-w.

Klein, F. W. *User's guide to HYPOINVERSE-2000, a Fortran program to solve for earthquake locations and magnitudes*. 2002. doi: 10.3133/ofr02171.

La Rocca, M., Creager, K. C., Galluzzo, D., Malone, S., Vidale, J. E., Sweet, J. R., and Wech, A. G. Cascadia Tremor Located Near Plate Interface Constrained by *S* Minus *P* Wave Times. *Science*, 323(5914):620–623, Jan. 2009. doi: 10.1126/science.1167112.

Luo, Y. and Ampuero, J. P. A model of spontaneous complex tremor migration patterns and background slow-slip events via interaction of brittle asperities and a ductile matrix. In *AGU Fall Meeting Abstracts*, volume 2014, pages S52B–01, 2014.

Luo, Y. and Ampuero, J.-P. Stability of faults with heterogeneous friction properties and effective normal stress. *Tectonophysics*, 733:257–272, May 2018. doi: 10.1016/j.tecto.2017.11.006.

Luo, Y. and Liu, Z. Rate-and-State Model Casts New Insight into Episodic Tremor and Slow-slip Variability in Cascadia. *Geophysical Research Letters*, 46(12):6352–6362, June 2019. doi: 10.1029/2019gl082694.

Luo, Y. and Liu, Z. Fault zone heterogeneities explain depth-dependent pattern and evolution of slow earthquakes in Cascadia. *Nature Communications*, 12(1), Mar. 2021. doi: 10.1038/s41467-021-22232-x.

Matharu, G., Bostock, M. G., Christensen, N. I., and Tromp, J. Crustal anisotropy in a subduction zone forearc: Northern Cascadia. *Journal of Geophysical Research: Solid Earth*, 119(9): 7058–7078, Sept. 2014. doi: 10.1002/2014jb011321.

Menant, A., Angiboust, S., and Gerya, T. Stress-driven fluid flow controls long-term megathrust strength and deep accretionary dynamics. *Scientific Reports*, 9(1), July 2019. doi: 10.1038/s41598-019-46191-y.

Menant, A., Angiboust, S., Gerya, T., Lacassin, R., Simoes, M., and Grandin, R. Transient stripping of subducting slabs controls periodic forearc uplift. *Nature Communications*, 11(1), Apr. 2020. doi: 10.1038/s41467-020-15580-7.

Merrill, R., Bostock, M. G., Peacock, S. M., Calvert, A. J., and Christensen, N. I. A Double Difference Tomography Study of the Washington Forearc: Does Siletzia Control Crustal Seismicity? *Journal of Geophysical Research: Solid Earth*, 125(10), Oct. 2020. doi: 10.1029/2020jb019750.

Nadeau, R. M. and Dolenc, D. Nonvolcanic Tremors Deep Beneath the San Andreas Fault. *Science*, 307(5708):389–389, Jan. 2005. doi: 10.1126/science.1107142.

Nedimović, M. R., Hyndman, R. D., Ramachandran, K., and Spence, G. D. Reflection signature of seismic and aseismic slip on the northern Cascadia subduction interface. *Nature*, 424(6947):

416–420, July 2003. doi: 10.1038/nature01840.

Nicholson, T., Bostock, M., and Cassidy, J. F. New constraints on subduction zone structure in northern Cascadia. *Geophysical Journal International*, 161(3):849–859, June 2005. doi: 10.1111/j.1365-246x.2005.02605.x.

Obana, K. and Kodaira, S. Low-frequency tremors associated with reverse faults in a shallow accretionary prism. *Earth and Planetary Science Letters*, 287(1–2):168–174, Sept. 2009. doi: 10.1016/j.epsl.2009.08.005.

Obara, K. Nonvolcanic Deep Tremor Associated with Subduction in Southwest Japan. *Science*, 296(5573):1679–1681, May 2002. doi: 10.1126/science.1070378.

Oncken, O., Angiboust, S., and Dresen, G. Slow slip in subduction zones: Reconciling deformation fabrics with instrumental observations and laboratory results. *Geosphere*, 18(1):104–129, Nov. 2021. doi: 10.1130/ges02382.1.

Peacock, S. M. Thermal and metamorphic environment of subduction zone episodic tremor and slip. *Journal of Geophysical Research: Solid Earth*, 114(B8), Aug. 2009. doi: 10.1029/2008jb005978.

Peacock, S. M., Christensen, N. I., Bostock, M. G., and Audet, P. High pore pressures and porosity at 35 km depth in the Cascadia subduction zone. *Geology*, 39(5):471–474, Mar. 2011. doi: 10.1130/g31649.1.

Peng, Y. and Rubin, A. M. High-resolution images of tremor migrations beneath the Olympic Peninsula from stacked array of arrays seismic data. *Geochemistry, Geophysics, Geosystems*, 17(2): 587–601, Feb. 2016. doi: 10.1002/2015gc006141.

Peng, Y., Rubin, A. M., Bostock, M. G., and Armbruster, J. G. High-resolution imaging of rapid tremor migrations beneath southern Vancouver Island using cross-station cross correlations. *Journal of Geophysical Research: Solid Earth*, 120(6):4317–4332, June 2015. doi: 10.1002/2015jb011892.

Plourde, A. P., Bostock, M. G., Audet, P., and Thomas, A. M. Low-frequency earthquakes at the southern Cascadia margin. *Geophysical Research Letters*, 42(12):4849–4855, June 2015. doi: 10.1002/2015gl064363.

Preston, L. A., Creager, K. C., Crosson, R. S., Brocher, T. M., and Trehu, A. M. Intraslab Earthquakes: Dehydration of the Cascadia Slab. *Science*, 302(5648):1197–1200, Nov. 2003. doi: 10.1126/science.1090751.

Rogers, G. and Dragert, H. Episodic Tremor and Slip on the Cascadia Subduction Zone: The Chatter of Silent Slip. *Science*, 300 (5627):1942–1943, June 2003. doi: 10.1126/science.1084783.

Roy, A., Roy, N., Saha, P., and Mandal, N. Factors Determining Shear-Parallel Versus Low-Angle Shear Band Localization in Shear Deformations: Laboratory Experiments and Numerical Simulations. *Journal of Geophysical Research: Solid Earth*, 126 (10), Oct. 2021. doi: 10.1029/2021jb022578.

Royer, A. and Bostock, M. A comparative study of low frequency earthquake templates in northern Cascadia. *Earth and Planetary Science Letters*, 402:247–256, Sept. 2014. doi: 10.1016/j.epsl.2013.08.040.

Royer, A. A., Thomas, A. M., and Bostock, M. G. Tidal modulation and triggering of low-frequency earthquakes in northern Cascadia. *Journal of Geophysical Research: Solid Earth*, 120(1): 384–405, Jan. 2015. doi: 10.1002/2014jb011430.

Rubin, A. M. and Armbruster, J. G. Imaging slow slip fronts in Cascadia with high precision cross-station tremor locations. *Geochemistry, Geophysics, Geosystems*, 14(12):5371–5392, Dec. 2013. doi: 10.1002/2013gc005031.

Saffer, D. M. and Tobin, H. J. Hydrogeology and Mechanics of Subduction Zone Forearcs: Fluid Flow and Pore Pressure. *Annual Review of Earth and Planetary Sciences*, 39(1):157–186, May 2011. doi: 10.1146/annurev-earth-040610-133408.

Sammis, C. G. and Bostock, M. G. A Granular Jamming Model for Low-Frequency Earthquakes. *Journal of Geophysical Research: Solid Earth*, 126(7), June 2021. doi: 10.1029/2021jb021963.

Savard, G. and Bostock, M. G. Detection and Location of Low-Frequency Earthquakes Using Cross-Station Correlation. *Bulletin of the Seismological Society of America*, 105(4):2128–2142, June 2015. doi: 10.1785/0120140301.

Savard, G., Bostock, M. G., and Christensen, N. I. Seismicity, Metamorphism, and Fluid Evolution Across the Northern Cascadia Fore Arc. *Geochemistry, Geophysics, Geosystems*, 19(6): 1881–1897, June 2018. doi: 10.1029/2017gc007417.

Scholz, C. H. Wear and gouge formation in brittle faulting. *Geology*, 15(6):493–495, 1987. doi: 0.1130/0091-7613(1987)15<493:WAGFIB>2.0.CO;2.

Schwartz, S. Y. and Rokosky, J. M. Slow slip events and seismic tremor at circum-Pacific subduction zones. *Reviews of Geophysics*, 45(3), Aug. 2007. doi: 10.1029/2006rg000208.

Shelly, D. R., Beroza, G. C., Ide, S., and Nakamula, S. Low-frequency earthquakes in Shikoku, Japan, and their relationship to episodic tremor and slip. *Nature*, 442(7099):188–191, July 2006. doi: 10.1038/nature04931.

Supino, M., Poiata, N., Festa, G., Vilotte, J. P., Satriano, C., and Obara, K. Self-similarity of low-frequency earthquakes. *Scientific Reports*, 10(1), Apr. 2020. doi: 10.1038/s41598-020-63584-6.

Supino, M., Shapiro, N. M., Vilotte, J.-P., Poiata, N., and Obara, K. Tectonic low-frequency earthquakes in Shikoku, Japan: source scaling, size distribution and observational limits. Mar. 2021. doi: 10.1002/essoar.10506594.1.

Sweet, J. R., Creager, K. C., Houston, H., and Chestler, S. R. Variations in Cascadia Low-Frequency Earthquake Behavior With Downdip Distance. *Geochemistry, Geophysics, Geosystems*, 20 (2):1202–1217, Feb. 2019. doi: 10.1029/2018gc007998.

Thomas, A. M., Nadeau, R. M., and Bürgmann, R. Tremor-tide correlations and near-lithostatic pore pressure on the deep San Andreas fault. *Nature*, 462(7276):1048–1051, Dec. 2009. doi: 10.1038/nature08654.

VanDecar, J. C. and Crosson, R. S. Determination of teleseismic relative arrival times using multi-channel cross-correlation and least-squares. *Bulletin of the Seismological Society of America*, 80:150–169, 1990.

Wech, A. G. Interactive Tremor Monitoring. *Seismological Research Letters*, 81(4):664–669, July 2010. doi: 10.1785/gssrl.81.4.664.

Wech, A. G. and Bartlow, N. M. Slip rate and tremor genesis in Cascadia. *Geophysical Research Letters*, 41(2):392–398, Jan. 2014. doi: 10.1002/2013gl058607.

Wech, A. G., Boese, C. M., Stern, T. A., and Townend, J. Tectonic tremor and deep slow slip on the Alpine Fault. *Geophysical Research Letters*, 39(10), May 2012. doi: 10.1029/2012gl051751.

Wells, R. E., Blakely, R. J., Wech, A. G., McCrory, P. A., and Michael, A. Cascadia subduction tremor muted by crustal faults. *Geology*, 45(6):515–518, Mar. 2017. doi: 10.1130/g38835.1.

Zhang, H. and Thurber, C. H. Double-Difference Tomography: The Method and Its Application to the Hayward Fault, California. *Bulletin of the Seismological Society of America*, 93(5): 1875–1889, Oct. 2003. doi: 10.1785/0120020190.